



**HAL**  
open science

## Angular resolved electron energy loss spectroscopy in hexagonal boron nitride

Frédéric Fossard, Lorenzo Sponza, Léonard Schué, Claudio Attaccalite, François Ducastelle, Julien Barjon, Annick Loiseau

► **To cite this version:**

Frédéric Fossard, Lorenzo Sponza, Léonard Schué, Claudio Attaccalite, François Ducastelle, et al.. Angular resolved electron energy loss spectroscopy in hexagonal boron nitride. 2017. hal-01439271v1

**HAL Id: hal-01439271**

**<https://hal.science/hal-01439271v1>**

Preprint submitted on 18 Jan 2017 (v1), last revised 6 Sep 2017 (v2)

**HAL** is a multi-disciplinary open access archive for the deposit and dissemination of scientific research documents, whether they are published or not. The documents may come from teaching and research institutions in France or abroad, or from public or private research centers.

L'archive ouverte pluridisciplinaire **HAL**, est destinée au dépôt et à la diffusion de documents scientifiques de niveau recherche, publiés ou non, émanant des établissements d'enseignement et de recherche français ou étrangers, des laboratoires publics ou privés.

# Angular resolved electron energy loss spectroscopy in hexagonal boron nitride

Frédéric Fossard,<sup>1</sup> Lorenzo Sponza,<sup>1</sup> Léonard Schué,<sup>1,2</sup> Claudio Attaccalite,<sup>3</sup> François Ducastelle,<sup>1</sup> Julien Barjon,<sup>2</sup> and Annick Loiseau<sup>1</sup>

<sup>1</sup>*Laboratoire d'Etude des Microstructures, ONERA-CNRS, UMR104, Université Paris-Saclay, BP 72, 92322 Châtillon Cedex, France*

<sup>2</sup>*Groupe d'Etude de la Matière Condensée, UVSQ-CNRS, UMR8635, Université Paris-Saclay, 45 avenue des Etats-Unis, 78035 Versailles Cedex, France*

<sup>3</sup>*Aix Marseille University and CNRS, CINAM, UMR7325, Campus de Luminy, case 913, 13288 Marseille, France*

(Dated: January 18, 2017)

Core and low energy electronic excitations have been studied in hexagonal boron nitride. Electron energy loss spectra have been measured using an electron microscope equipped with a monochromator and an in-column filter. Energy filtered diffraction patterns have been recorded and provide us with a global view of anisotropic effects in reciprocal space. From combined angular and energy resolved measurements, we analyze the symmetry of the losses as a function of the energy transferred to the material. As an example we show how easily the core loss spectra at the  $K$  edges of boron and nitrogen can be measured and imaged. Low losses associated to interband and/or plasmon excitations are also measured and discussed from *ab initio* calculations. This electronic inelastic scattering technique is shown to provide results comparable to those obtained from non resonant X-ray inelastic scattering. Both techniques are complementary: X-ray scattering is more accurate at large  $\mathbf{q}$  wave vector whereas electron spectroscopy is more accurate at low  $\mathbf{q}$  and is an attractive tool to study excitonic effects, which are inaccessible by optical techniques. Furthermore the method is fast and local, at a nanoscale level, and is very promising for studying two dimensional materials and related heterostructures.

## I. INTRODUCTION

Two-dimensional (2D) materials are currently the object of many investigations concerning their electronic and optical properties. Graphene is a well-known example<sup>1</sup> but hexagonal boron nitride ( $h$ -BN)<sup>2-7</sup> and now transition metal dichalcogenides<sup>8-12</sup> as well as new materials such as phosphorene,<sup>13,14</sup> silicene, or germanene, are receiving considerable attention. Unlike graphene, these materials are semiconductors with optical properties dominated by excitonic effects which depend on the number of layers and on the nature of the layer stacking.<sup>15</sup>

In this landscape,  $h$ -BN displays a singular situation since it is a large band gap (about 6 eV) semiconductor with a honeycomb lattice similar to that of graphene where boron and nitrogen alternate at the vertices of the honeycomb lattice. Optical measurements on  $h$ -BN are difficult because of the necessity to work in the far UV range and require dedicated laser sources and detection devices.<sup>2-4,16</sup> Another possibility is to excite the system with electrons and to perform cathodoluminescence experiments.<sup>6,7,17,18</sup> Finally photoemission excitation spectra can be obtained using VUV synchrotron radiation excitation.<sup>5</sup> All these experiments have clearly shown the importance of excitonic effects in agreement with several theoretical studies<sup>19-24</sup> although their exact nature remains far from being fully clarified.

To go further in understanding excitonic properties, inelastic scattering techniques are useful and complementary tools to the above cited optical spectroscopies. It is recalled here that the response to electronic excita-

tions is characterized by the dynamical structure factor  $S(\mathbf{q}, \omega)$  which is itself related to the dielectric response  $\varepsilon(\mathbf{q}, \omega)$ , where  $\omega$  and  $\mathbf{q}$  are the energy (or frequency) and momentum variations during the involved scattering process.<sup>25,26</sup> As far as energy is concerned, optical techniques (absorption, photoluminescence) are very accurate but are confined to the  $\mathbf{q} \rightarrow 0$  limit. Recently performing non resonant inelastic x-ray scattering (NRIXS) experiments on  $h$ -BN single crystals, the full Brillouin zone (and beyond) could be explored and energy losses were recorded between a few eV and 40 eV. At low energy the energy resolution (down to 200 meV) made accessible the investigation of the near edge excitonic regime for different values of  $\mathbf{q}$ .<sup>27,28</sup>

Such experiments can also be performed by using inelastic scattering of fast electrons (electron energy loss spectroscopy (EELS)). This technique has suffered for a long time of a low energy resolution. This is no longer the case with the latest generations of electron microscopes and these methods can now be used to investigate not only the core loss regime where energy variations are in the range  $10^2 - 10^3$  eV but also the low loss regime,  $\omega = 1 - 50$  eV. The current implantation of electron spectroscopy in transmission electron microscopes makes this technique particularly attractive as it allows one to perform local investigations at the nanoscale, with no need of large samples and with access to the impact of defects on the spectroscopic properties.

In this article we present results of a detailed EELS study of  $h$ -BN using a transmission electron microscope (TEM) designed for performing angular resolved electron spectroscopy. We show that the results are similar to

those obtained using synchrotron x-ray sources (NRIXS) in terms of energy resolution, with the advantage to obtain also global maps of  $S(\mathbf{q}, \omega)$  in the diffraction plane and to have a privileged access to the small  $\mathbf{q}$  region of the Brillouin zone. The method is fast and can be applied to small samples. This opens the way to a broad field of applications, to 2D materials and their heterostructures. The methods are described in Sec.II. The results are presented in Sec. III, those for the core loss spectra at the boron  $K$  edge in Sec. IIIA and those for the low loss spectra in Sec. IIIB. Further documentation can be found in the Supplemental Material.

## II. TEM-EELS EXPERIMENTS

In the past decade, the development of aberration corrected TEM has brought new tools to the scientific community which are particularly suited to image thin materials.<sup>29,30</sup> Moreover, with the improvement of electron sources and monochromators associated with optimized spectrometers, EELS spectra can be recorded with atomic and sub-eV energy resolutions.<sup>31,32</sup> However such systems still make compromises in order to increase the signal by integrating over a finite collecting solid angle<sup>30</sup> or by shining the sample with a very focused beam with a large illumination angle so that the angular dependent information is averaged or truncated.<sup>33</sup> The techniques used here avoid these disadvantages. They combine energy filtered TEM (EFTEM) and EELS. The electron microscope is a Zeiss Libra 200 MC equipped with an electrostatic CEOS monochromator, an in-column  $\Omega$  filter and a Gatan ultrascan 1000 CCD camera. The microscope operates at 80 kV and the monochromated beam gives a resolution of 100 meV with the narrowest slit. The Köhler illumination ensures that the beam is parallel, and that its convergence is kept below 80  $\mu$ rad.

To measure the dynamical structure factor it is convenient to work within the diffraction plane of the microscope where the scattering angles can be related to the transferred momenta. Since the transferred momentum is much smaller than the momentum of the incoming beam, the relation between them is given by  $q^2 \simeq k^2(\theta^2 + \theta_E^2)$ , where  $\mathbf{k}$  is the initial momentum,  $\theta$  is the scattering angle and  $\theta_E$  is proportional to the energy loss.<sup>25</sup> For a given orientation of the sample, a data cube is built from the values of  $\omega$ ,  $q_x$  and  $q_y$ , the incident beam being along the  $z$  direction.<sup>34</sup> The component along this direction,  $q_E = k\theta_E$  is negligible in general, except when  $q$  is close to zero. This is illustrated in Fig. 1.

Two strategies have been applied to record this information and are described below. A first method consists in recording scattering patterns at given energy losses and to stack them in order to build the horizontal slices of the datacube. The main advantage of this procedure is to obtain the  $q_x$  and  $q_y$  values of the transferred momentum with the same resolution. The spectral resolution of the EFTEM experiment is determined by the

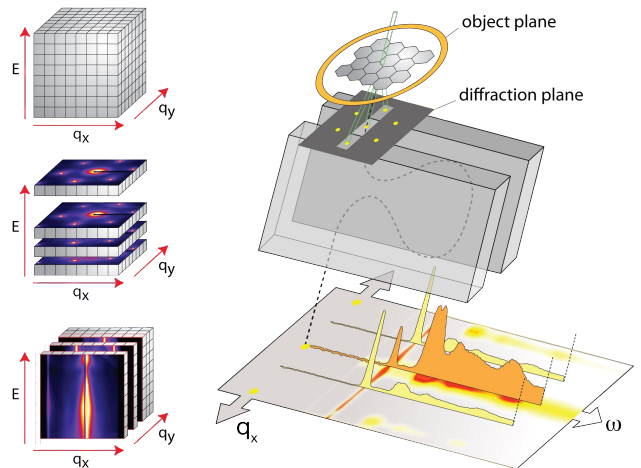


FIG. 1. Upper left : datacube in reciprocal space ; middle left :  $(E, q_x, q_y)$  datacube construction in EFTEM ; bottom left :  $(E, q_x, q_y)$  datacube construction in  $\omega - \mathbf{q}$  map. Right : schematic principle of the  $\omega - \mathbf{q}$  map acquisition.

exit slit of the energy filter which selects a bandwidth in the energy-selecting plane.<sup>35</sup> The filtered electrons within this bandwidth form the scattering pattern. The intensity of the signal is an order of magnitude lower than the intensity of a usual diffraction pattern. As a consequence, the integrating time to record one slice is usually larger than 10 s. Data are measured every 0.25 eV to get a smooth spectrum which is used to subtract a power law background in the  $\omega$  direction of the data cube for every  $(q_x, q_y)$  pixel.

In order to take full advantage of the monochromator and to obtain more quantitative results on the double  $\omega - \mathbf{q}$  dependence, a second method is to combine the imaging capabilities of the projective system with the energy dispersion generated by the  $\Omega$  energy filter in the microscope. A rectangular slit can be placed at the entrance of the filter in order to select a direction in reciprocal space.<sup>36,37</sup> The orientation of the slit is fixed and its larger dimension is perpendicular to the direction of the energy dispersion. The orientation of the sample must be adjusted in order to align the slit with a specific crystallographic direction. This can be done using a tilt/rotation holder ensuring a 360° rotation around the optical axis. Furthermore, since the slit is placed after the first projective system of the microscope, we can also rotate the diffraction pattern by changing the camera length.

The multipoles of the filter must be adjusted in order to keep the  $q_x$  information in the direction of the slit while dispersing the energy of the electrons. The image recorded on the camera is therefore in the  $(q_x, \omega)$  plane as illustrated in Fig. 1 (right). Thus, by shifting the scattering pattern with the first projector system, we can scan the  $q_y$  direction using discrete steps. In other words, the data cube is now built with vertical slices as illustrated in Fig. 1 (bottom left).

It is worth noting that the  $\mathbf{q}$ -resolution in both experiments depends on several instrumental parameters as well as on sample specifications. Indeed, both experiments are diffraction experiments and the broadening of the signal is related to the illumination angle, the camera length used, the optical design of the column, the width of slits and apertures.<sup>37</sup> One should also take into account the crystallinity of the sample over the diffracting area. In our case, the area is delimited by an aperture which gives a virtual circular area with a diameter of 70 nm. It will be shown below, in Sec. III, that the resolution along  $q_x$  can be estimated about a few  $10^{-2} \text{ \AA}^{-1}$ , whereas the thickness of the slice along  $q_y$  in the  $\omega - \mathbf{q}$  mode is about  $0.2 \text{ \AA}^{-1}$ .

The procedures described above necessitate to have  $h$ -BN samples with well defined orientations. Three slabs have been cut by focused ion beam from a  $h$ -BN single crystal<sup>38</sup> along  $(0001)$ ,  $(10\bar{1}0)$  and  $(11\bar{2}0)$  crystallographic planes whose normals are the  $\Gamma A$ ,  $\Gamma M$  and  $\Gamma K$  directions in the first Brillouin zone (see Fig. 2). Details are given in the Supplemental Material.

### III. RESULTS

#### A. Core losses at the boron $K$ edge

Studying electron energy loss (EEL) at the boron  $K$ -edge is a textbook case for illustrating the potentialities of our technique. The different peaks are sharp and related to well-known transitions with typical symmetries between the deep  $1s$  level and the first unoccupied  $\pi^*$  states (192 eV) and  $\sigma^*$  states (199 eV).<sup>39–46</sup> Energy filtered scattering patterns have been recorded in the 185–215 eV range for the three samples. Fig. 2 presents the elastic diffraction pattern of the second sample with labeled directions as well as inelastic filtered patterns at the  $1s \rightarrow \pi^*$  energy (192 eV) and the one close to the  $1s \rightarrow \sigma^*$  energy (200 eV) obtained by EFTEM. Notice that in both cases diffuse intensities also occur around the Bragg peaks. This is due to double-scattering processes involving inelastic scattering and elastic Bragg scattering. At 192 eV, all diffraction spots are splitted into two symmetric lobes with the specific  $[0001]$  orientation (along the axis of the hexagonal cell). The corresponding  $\omega - \mathbf{q}$  plot in the  $\Gamma A$  direction is shown in Fig. 3. We have a clear illustration here of the anisotropy of the losses in the  $1s \rightarrow \pi^*$  transition, which can simply be explained as follows.<sup>39,45</sup>

In the simplest single-electron picture the dynamic structure factor is given by:

$$S(\mathbf{q}, \omega) = \sum_f |\langle f | e^{i\mathbf{q}\cdot\mathbf{r}} | i \rangle|^2 \delta(E_f - E_i - \hbar\omega), \quad (1)$$

where  $i$  and  $f$  denote the one-electron initial and final states, respectively, the differential cross section  $d^2\sigma/d\Omega dE$  for electron scattering being equal to

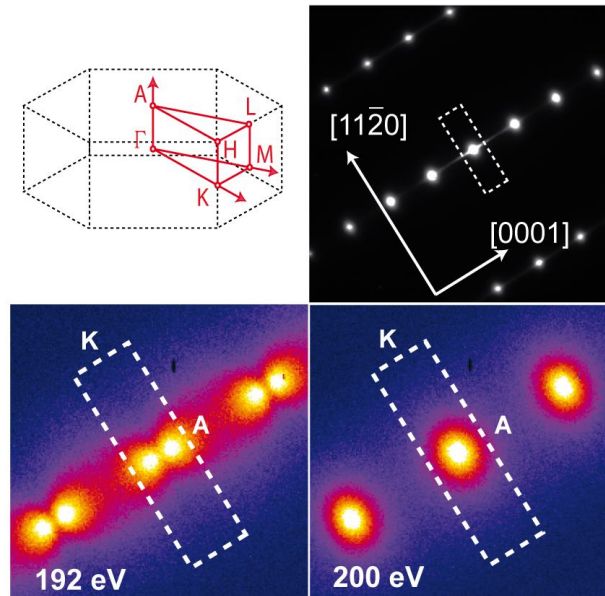


FIG. 2. Top: Hexagonal Brillouin zone and diffraction pattern of  $h$ -BN in a plane containing the hexagonal axis (direction  $\Gamma A$ ) and the  $\Gamma K$  direction. Bottom: Energy filtered scattering patterns recorded at 192 eV (left) and at 200 eV (right).

$4S(\mathbf{q}, \omega)/(a_0^2 q^4)$ , where  $a_0$  is the Bohr radius. The matrix element  $\langle f | e^{i\mathbf{q}\cdot\mathbf{r}} | i \rangle$  reduces here to the matrix element between the core boron  $1s$  function and the conduction band states. In the case of  $h$ -BN the conduction states at low energy are concentrated on the boron atoms, and more precisely on their  $\pi_{||}$  states pointing along the hexagonal axis,<sup>24</sup> so that finally, within the dipolar approximation, we have to calculate the dipolar matrix element  $\langle \pi_{||} | \mathbf{q}\cdot\mathbf{r} | 1s \rangle$ . Because of the symmetry of the  $\pi_{||}$  state, only the component of  $\mathbf{r}$  along the hexagonal axis survives, so that we expect that  $S(\mathbf{q}, \omega)/q^4 \simeq q_{||}^2/q^4 = \cos^2 \alpha/q^2$ , where here  $\alpha$  is the angle between  $\mathbf{q}$  and the hexagonal axis.<sup>39</sup> This means that the symmetry of the scattered intensity around the origin should be similar to that of the  $\pi$  electron density itself. This is clearly the case as shown in Fig. 2 and in Fig. 4 where an enlargement of the central lobes is shown.

More precisely let us decompose the scattering wave vector  $\mathbf{q}$  into its component in the diffraction plane  $\bar{\mathbf{q}}$  and its inelastic component  $\mathbf{q}_E$  along the incident beam, normal to this plane.<sup>37</sup> Then the scattering cross section measured in the diffraction plane is proportional to

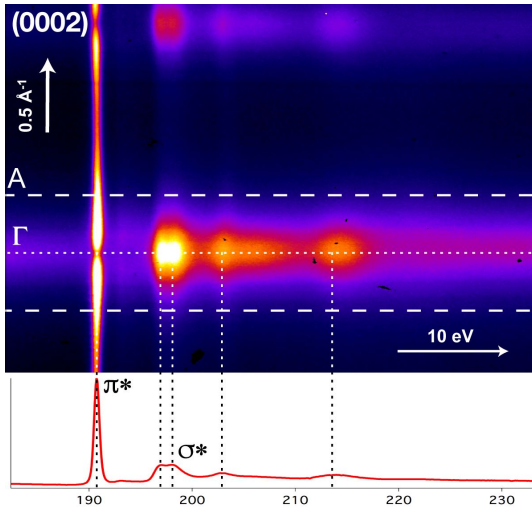


FIG. 3. Top:  $\omega - \mathbf{q}$  image recorded in the  $\Gamma A$  direction close to the boron  $K$ -edge energy. Dashed lines delimitate the Brillouin zone. Bottom : related EELS spectrum integrated over the whole Brillouin zone. Dotted lines indicate the Brillouin zone section and significant edge structures.

$\bar{q}^2 \cos^2 \alpha / (\bar{q}^2 + q_E^2)^2$ . This induces an intensity dip along the hexagonal lattice, of width equal to  $2q_E$ , when approaching the origin. Actually, in this limit  $\bar{q} \rightarrow 0$ , the scattering vector is normal to the diffraction plane and therefore in the nodal plane of the  $\pi$  orbital. We can calculate  $q_E$ , equal to  $E/\hbar v_0$  where  $E$  is the energy loss and  $v_0$  the electron velocity determined by the accelerating tension of the microscope. In our case,  $q_E \simeq 0.20 \text{ \AA}^{-1}$ , and it can be seen in Fig. 4 that the above formula fits perfectly the measured profiles. This indicates that the (angular) resolution in  $q$ -space is very good. It is estimated to a few  $10^{-2} \text{ \AA}^{-1}$ .

At higher energy (200 eV) the diffraction pattern is modified with an intensity much more isotropic and with an extension in the basal plane typical of the appearance of  $\sigma$  states, as also discussed by Leapman et al.<sup>39</sup>

The difference between the two regimes is even more obvious when looking at the  $\omega - \mathbf{q}$  plot shown in Fig. 3. It can be noticed that the  $\pi^*$  peak at low energy is separated from a quasi-continuum starting at higher energy in correspondence with the  $\sigma^*$  peak, which is typical of an excitonic behaviour. The splitting of the main  $\sigma^*$  peak, apparent in the  $\omega - \mathbf{q}$  plot has probably also an excitonic origin.<sup>47</sup> The corresponding EEL spectrum for  $\bar{q}$  along the hexagonal axis is shown in Fig. 4. Actually the presence of a core hole is important here and the single electron description should be improved. This has been done, in particular in Ref. [45] where the authors calculate the full dielectric constant using the Bethe Salpeter formalism<sup>48</sup> and found good agreement with the experimental data.

$\omega - \mathbf{q}$  plots have also been obtained for energies close to the nitrogen K edge (see Supplemental Material).

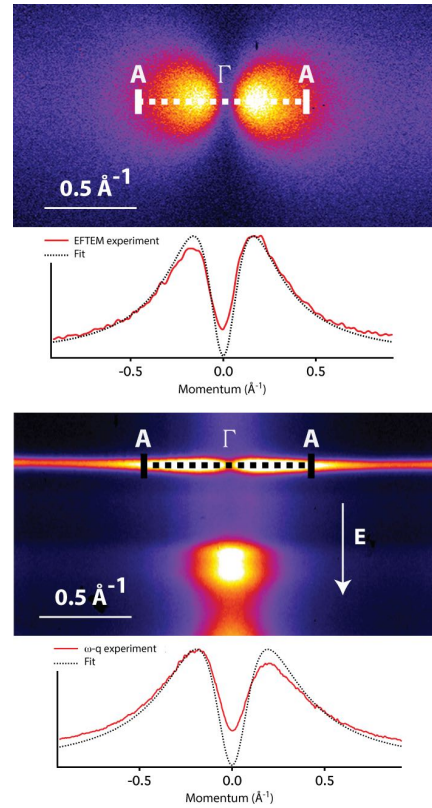


FIG. 4. Enlargement of the inelastic scattered intensity corresponding to the  $\sigma \rightarrow \pi^*$  transition and related profile in the  $\Gamma A$  direction in EFTEM at 192 eV (left) and  $\omega - \mathbf{q}$  plot (right). The fit is made using a profile function proportional to  $\bar{q}^2 / (\bar{q}^2 + q_E^2)^2$  with  $q_E = 0.20 \text{ \AA}^{-1}$ .

Then the core hole is on the nitrogen atom, but the electron in the conduction band is still concentrated on the boron atoms. Excitonic effects and oscillator strengths are therefore expected to be weaker, which is the case: The measured EELS signals are much weaker and then less accurate, and the spectra show broader and less “atomic-like” features, in agreement with previous studies.<sup>41,42,44,47,49</sup>

## B. Low loss region

The low loss regime is related to the loss function, equal to  $-\text{Im}(1/\varepsilon(\mathbf{q}, \omega))$  proportional to  $S(\mathbf{q}, \omega)/q^2$ , so that the differential scattering cross section is proportional to  $-1/q^2 \text{Im}(1/\varepsilon(\mathbf{q}, \omega))$ . The peaks of the loss function are frequently associated with plasmons. Two energy ranges are generally distinguished, with a  $\pi$  plasmon peak in the 6–8 eV range and a  $\sigma + \pi$  peak at about 25 eV for bulk  $h$ -BN and also for graphite,<sup>50–54</sup> the position and the intensity of the latter peak being strongly dependent on the number of sheets for thin samples. The position of some structures can also be associated to specific in-

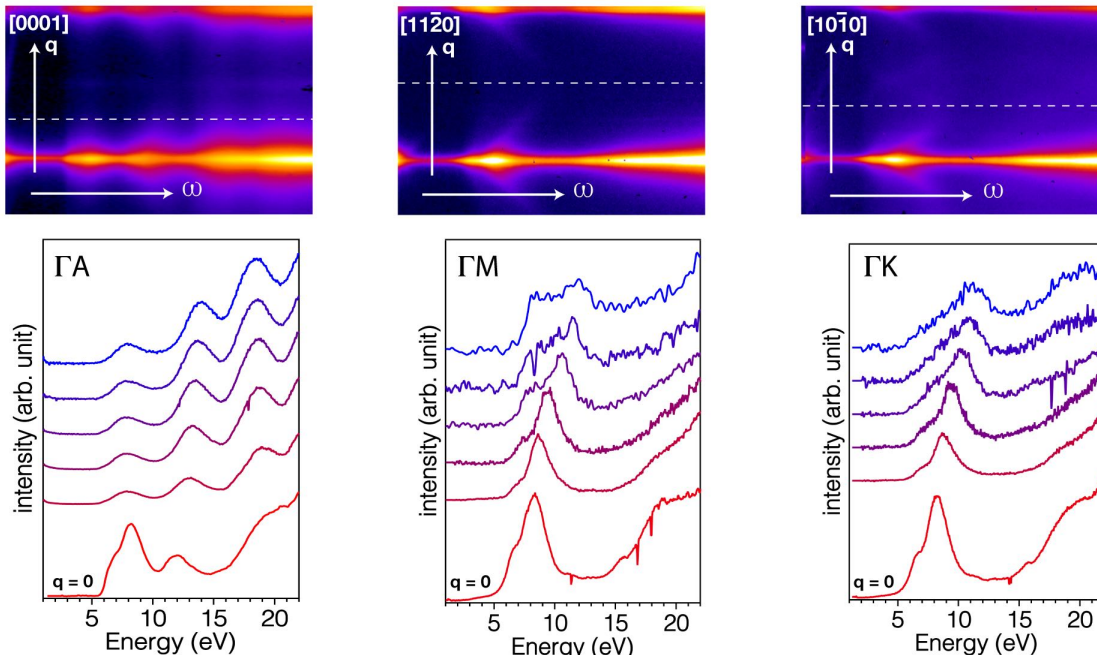


FIG. 5.  $\omega - \mathbf{q}$  plots (top panels) and EELS spectra (bottom panels) along the three  $\Gamma A$ ,  $\Gamma M$  and  $\Gamma K$  directions. When  $q \neq 0$ , the EELS have been multiplied by  $q^2$ . The spectra for  $q = 0$  are shown separately. The other are distributed every 20% of the Brillouin zone. The dotted lines in the  $\omega - \mathbf{q}$  plots indicate the Brillouin zone boundaries.

terband transitions, particularly if they are correlated to the behaviour of  $\epsilon(\mathbf{q}, \omega)$  itself through Kramers-Kronig analyses,<sup>50</sup> but some controversy has appeared recently between these two interpretations and concerning the nature of the observed signals in 2D systems such as graphene.<sup>55–58</sup> It is not obvious actually to derive well-defined dispersion relations and to decide between the two possibilities. In most cases the excitations have a mixed character reinforced by the fact that local field and many-body effects are important, so that the discussion has a somewhat semantic character. On the other hand, accurate calculations based on the Bethe-Salpeter equation are now available and allow us to compare them with the experimental results. This has been successfully achieved recently using NRIXS.<sup>27,28</sup> We show below that our EELS experiments are in good agreement with these works and that they provide useful complementary information.

$\omega - \mathbf{q}$  plots as well as EELS plots in the three  $\Gamma A$ ,  $\Gamma M$  and  $\Gamma K$  directions have been obtained and are shown in Fig. 5 in the range 0–25 eV. They are comparable with NRIXS measurements and theoretical calculations in literature<sup>27,28</sup> (see Supplemental Material), which we summarize. Along  $\Gamma K$  the low energy peak moves upwards, from about 8 eV to about 12 eV whereas along

$\Gamma M$  this peak splits when  $q$  approaches the Brillouin zone boundary at  $M$  ( $q = 1.45 \text{ \AA}^{-1}$ ). Along  $\Gamma A$  the peak positions at about 8 eV and 12 eV do not move significantly with  $q$ , which reflects the fact that the hexagonal planes weakly interact.

### 1. Low $q$ limit

Let us now discuss in more detail the low  $q$  limit. This regime is particularly relevant since the cross section varies as  $1/q^2$  in EELS, whereas it goes as  $q^2$  in NRIXS, which makes the former technique well suited to probe small exchanged momenta. When comparing  $\Gamma K$  and  $\Gamma M$  directions it is clear that the scattered intensity becomes isotropic in the basal plane when  $q \rightarrow 0$ , as expected,  $\epsilon(\mathbf{q}, \omega) \rightarrow \epsilon_{\perp}(\omega)$ . The intensity along  $\Gamma A$  is different as expected also since then  $\epsilon(\mathbf{q}, \omega) \rightarrow \epsilon_{\parallel}(\omega) \neq \epsilon_{\perp}(\omega)$ . On the other hand the spectrum at vanishing  $q$  shows a low energy peak at 8 eV which looks similar to that observed in the basal plane. This is surprising since most calculations predict a negligible intensity below 12 eV for  $\epsilon_{\parallel}(\omega)$ .<sup>52,59,60</sup>

The point is that we have to be careful in this limit. In the case of core losses, this was because of the importance

of the  $q_E$  component. Here because of the lower energy loss,  $q_E$  is much smaller, of the order of  $0.005 \text{ \AA}^{-1}$ , but the problem comes from the width  $\Delta q_y$  of the slit used in the  $\omega - \mathbf{q}$  mode which is about  $0.20 \text{ \AA}^{-1}$ . Here the  $q_y$  direction is within the basal plane, in the  $\Gamma M$  direction, so that what is measured in the  $q \rightarrow 0$  limit is a mixture of contributions related to  $\varepsilon_{\parallel}(\omega)$  and  $\varepsilon_{\perp}(\omega)$ , the latter being predominant.

### 2. Low energy limit

Let us discuss more precisely the behaviour of the spectra close to the low energy edge where excitonic effects are the most important. From optical measurements we know that for  $\mathbf{q} = 0$  the electron-hole excitation spectrum presents an exciton state fairly localized within the hexagonal planes, with a bonding energy about 1 eV. On the other hand step-like singularities at the low energy edge are clearly visible in Fig. 5 when  $\mathbf{q} = 0$  in the basal plane ( $\Gamma K$  and  $\Gamma M$  directions). Since the exciton bound state should induce a peak slightly above it in the loss function, this step is an excitonic signature, which clearly disperses upwards when  $\mathbf{q}$  increases, as expected. This assignment is also confirmed from an analysis of theoretical curves (see Supplemental Material).

Along  $\Gamma A$  the situation is more complex in the  $q \rightarrow 0$  limit as mentioned above. The ground state exciton which is polarized in the basal plane is dark in principle along  $\Gamma A$ . Other bright excitons, extended on several planes, are expected a few tenths of eV above it<sup>27</sup> but the experimental resolution is still not sufficient to see them.

### 3. Comparison with theoretical calculations

As discussed by Galambosi *et al.*<sup>27</sup> and by Fugallo *et al.*,<sup>28</sup> several theoretical ingredients are necessary to account for all the details of the inelastic scattering experiments. In the three panels of Fig. 6 we compare, at points  $A$ ,  $M$ , and  $K$  of the Brillouin zone, our experimental data with *ab-initio* spectra obtained in the random phase approximation (RPA) and solving the Bethe-Salpeter equation (BSE).

The structural parameters used in the simulations of the hexagonal cell of  $h$ -BN are  $a=2.50 \text{ \AA}$  and  $c=6.5 \text{ \AA}$ , in agreement with those obtained from measured diffraction patterns. The ground state density has been obtained sampling the Brillouin zone with a  $(6 \times 6 \times 2)$   $\Gamma$ -centred  $k$ -point grid and including plane waves up to 900 eV. The Perdew-Burke-Ernzerhof approximation has been adopted for the exchange-correlation potential.<sup>61</sup> The RPA loss function spectra have been computed in all  $q$ -points of a  $(24 \times 24 \times 8)$   $\Gamma$ -centred grid, including 20 bands and with a cutoff of 60 eV. The maps at energy  $E$  reported in Fig. 8 have been obtained by first averaging the computed spectra in the range  $E \pm 0.5 \text{ eV}$

and then interpolating the result on a sufficiently dense mesh (50 points). The BSE has been solved for six valence bands and eight conduction bands with a scissor operator of 1.73 eV (derived from the average GW correction across the gap) on a  $(12 \times 12 \times 4(8))$   $\Gamma$ -centred  $q$ -point grid for  $\mathbf{q}$  in-plane (out-of-plane). A cutoff of 60 eV and 20 bands have been included to converge the dielectric constant entering in the direct term of the excitonic Hamiltonian. All spectra have been convoluted with a gaussian of width 0.2 eV. All calculations have been carried out with the code GPAW.<sup>62</sup>

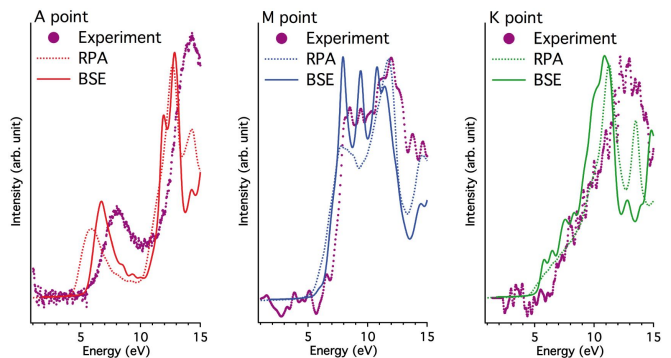


FIG. 6. Comparison between the present EELS data and theoretical (RPA and BSE) calculations.

Our experimental data compare well with the BSE calculations, confirming the excitonic nature of several spectral features, as pointed out in similar previous studies.<sup>27,28</sup> The comparison between RPA and BSE calculations can help in individuating them. More details on the analysis of theoretical curves are given in the Supplemental Material. It is worth noticing that at  $\mathbf{q} = M$  and  $\mathbf{q} = K$  the peaks of the RPA and the BSE calculations fall almost at the same place, and similarly the onset. This indicates that for in-plane perturbations the electron-hole interaction and the quasiparticle correction (here approximated by a scissor operator) almost cancel mutually. The result is that simple RPA calculations reproduce fairly well the measured loss function for in-plane momentum transfer. Instead, for  $\mathbf{q} = A$ , the onset is clearly blue-shifted by about 0.8 eV indicating a weaker exciton binding energy close to the onset. At higher energies, the difference between electron-hole interaction and quasiparticle corrections is reduced and they cancel close to 12 eV.

### 4. Scattering patterns

It is also instructive to look at the scattering patterns taken at different energies. We first show in Fig. 7 a view

of a large part of reciprocal space taken at 8 eV and 12 eV in order to illustrate the importance of multiple scattering effects which clearly mask the details of the diffuse intensity which is the relevant quantity here. This forbids any quantitative analysis beyond the first Brillouin zone. In Fig. 8, we have then considered the first Brillouin zone and compared the experimental pattern to the theoretical one obtained from RPA calculations. As seen before, for in-plane components there is a mutual cancellation of one-particle and two-particle processes which justifies the use of a simpler approximation. The patterns are obtained with a fairly broad energy window, about 1 eV. The agreement is very good.

At low energy (8 eV), the patterns in the  $\Gamma KM$  plane are characterized by an intensity concentrated at the origin, with diffuse arms pointing along the  $\Gamma M$  directions, whereas at higher energy the intensity is higher close to the Brillouin zone boundary, with diffuse arms along the  $\Gamma K$  directions. This is consistent with a simple analysis in terms of  $\pi - \pi^*$  excitations in this energy regime. At low energy the transitions are mainly direct transitions ( $q \simeq 0$ ), whereas they are indirect at higher energy.<sup>27</sup>

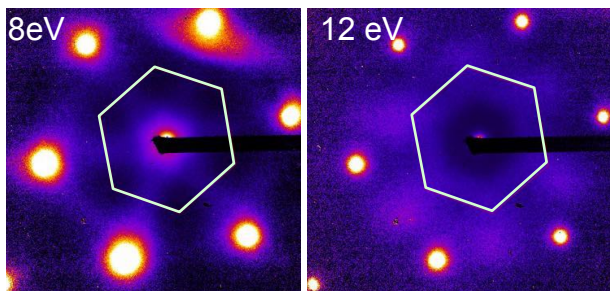


FIG. 7. Energy filtered scattering patterns at different energies in the low loss regime. The intensities are multiplied by  $q^2$ . White lines delimitate the Brillouin zone.

At the bottom of Fig. 8, we show similar maps at 12 eV in the  $\Gamma AM$  plane which contains therefore the  $\Gamma A$  direction. As expected from the spectra in Fig. 5 the intensity at low  $q$  is maximum in the  $\Gamma A$  direction. In drawing the  $\Gamma AM$  maps, one has to treat parallel and perpendicular components on the same footing. As stressed in the previous section, the agreement between RPA spectra and experiment is comparable in the two directions around 12 eV, which is not the case at lower energy where accurate BSE calculations (under progress) are necessary.

#### IV. CONCLUSION

In summary, we have shown by treating the case of  $h$ -BN, that momentum-resolved EELS allows us to obtain accurate information on the electronic excitation spectra for core losses as well as for low losses. The energy filtered diffraction patterns provide a global view of anisotropy effects in  $q$  space, whereas the  $\omega - q$  plots allow us to

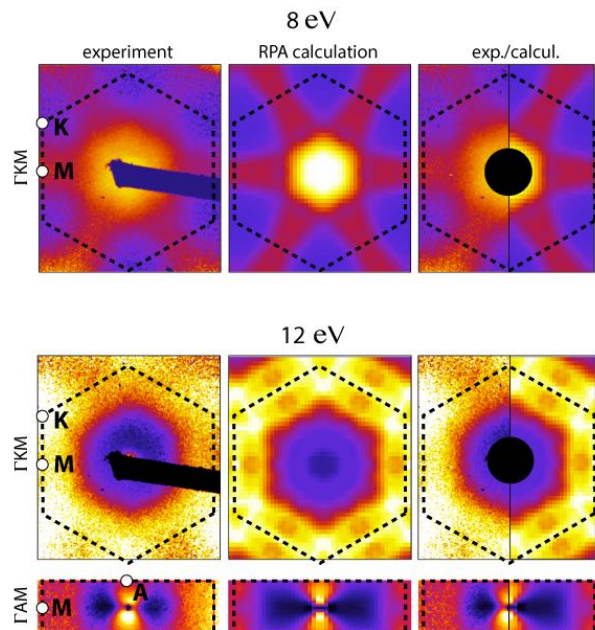


FIG. 8. Experimental and calculated loss functions (scattered intensities multiplied by  $q^2$ ) at 8 eV for the  $\Gamma KM$  plane and at 12 eV for the  $\Gamma KM$  and  $\Gamma AM$  planes. Dashed lines delimitate the Brillouin zone.

map the symmetries of the losses as a function of the energy transferred to the material. The case of core losses related to the excitonic  $\sigma - \pi^*$  transitions at the boron  $K$  edge has been shown to be particularly spectacular. In the case of low losses, our results confirm those of inelastic x-ray scattering experiments and of theoretical analyses taking into account excitonic effects within the Bethe Salpeter formalism.

EELS is therefore an efficient technique complementary of other inelastic scattering tools such as NRIXS. Let us compare them in more detail. The energy resolutions are similar, about 100-200 meV, but their accuracy in  $q$ -space is different. Actually, as already mentioned before, the scattering cross section is proportional to  $q^2 \text{Im}(-1/\epsilon(\mathbf{q}, \omega))$  in the case of NRIXS, and proportional to  $(1/q^2) \text{Im}(-1/\epsilon(\mathbf{q}, \omega))$  in the EELS case. The latter is more accurate at small  $q$ , the former at large  $q$ . This has been already nicely analysed by Weissker *et al.*<sup>63</sup> At large  $q$ , as mentioned by these authors, “the EELS results are plagued by multiple scattering.” We have shown that this is actually the case and NRIXS is much better to analyse features outside the first Brillouin zone, as described recently.<sup>28</sup> On the other hand EELS is

much better at low  $q$  which opens the way to make contact with optical measurements. The latter have a good energy resolution but are confined to  $q \simeq 0$ . In the case of 2D materials where excitonic effects are important it will therefore be very useful to have a tool to measure the dispersion as a function of  $q$  of the excitonic levels. EELS within an electron microscope has also the specific advantage to permit fast and local experiments at the nanoscale.

## ACKNOWLEDGMENTS

T. Taniguchi and K. Watanabe from NIMS are warmly acknowledged for providing a reference HPHT crystal. The authors want to thank David Troadec from IEMN for the FIB samples preparation, and Philip Wachsmuth, Gerd Benner and Ute Kaiser for very useful discussions on  $\omega - q$  maps. Hakim Amara is acknowledged for many fruitful discussions, Giorgia Fugallo for the careful comparison with her theoretical results, and Etienne Gaufrès for a careful reading of the manuscript. The research leading to these results has received funding from the European Union H2020 Programme under grant agreement no. 696656 GrapheneCore1. We acknowledge funding by the French National Research Agency through Project No. ANR-14-CE08-0018.

- 
- <sup>1</sup> A. H. Castro Neto, F. Guinea, N. M. R. Peres, K. S. Novoselov, and A. K. Geim, "The electronic properties of graphene," *Rev. Mod. Phys.* **81**, 109–162 (2009).
  - <sup>2</sup> Kenji Watanabe, Takashi Taniguchi, and Hisao Kanda, "Direct-bandgap properties and evidence for ultraviolet lasing of hexagonal boron nitride single crystal," *Nature Materials* **3**, 404–9 (2004).
  - <sup>3</sup> P. Jaffrennou, J. Barjon, J.-S. Lauret, A. Loiseau, F. Ducastelle, and B. Attal-Tretout, "Origin of the excitonic recombinations in hexagonal boron nitride by spatially resolved cathodoluminescence spectroscopy," *Journal of Applied Physics* **102**, 116102 (2007).
  - <sup>4</sup> K. Watanabe and T. Taniguchi, "Jahn-Teller effect on exciton states in hexagonal boron nitride single crystal," *Physical Review B* **79**, 193104 (2009).
  - <sup>5</sup> L. Museur, G. Brasse, A. Pierret, S. Maine, B. Attal-Tretout, F. Ducastelle, A. Loiseau, J. Barjon, K. Watanabe, T. Taniguchi, and A. Kanaev, "Exciton optical transitions in a hexagonal boron nitride single crystal," *Phys. status solidi - Rapid Res. Lett.* **5**, 214–216 (2011).
  - <sup>6</sup> A. Pierret, J. Loayza, B. Berini, A. Betz, B. Plaçais, F. Ducastelle, J. Barjon, and A. Loiseau, "Excitonic recombinations in hBN : From bulk to exfoliated layers," *Physical Review B* **89**, 035414 (2014).
  - <sup>7</sup> Leonard Schue, Bruno Berini, Andreas C. Betz, Bernard Plaçais, Francois Ducastelle, Julien Barjon, and Annick Loiseau, "Dimensionality effects on the luminescence properties of hbn," *Nanoscale* **8**, 6986–6993 (2016).
  - <sup>8</sup> W. Zhao, Z. Ghorannevis, L. Chu, M. Toh, C. Kloc, P.-H. Tan, and G. Eda, "Evolution of Electronic Structure in Atomically Thin Sheets of WS<sub>2</sub> and WSe<sub>2</sub>," *ACS Nano* **7**, 791–7 (2012).
  - <sup>9</sup> Mingsheng Xu, Tao Liang, Minmin Shi, and Hongzheng Chen, "Graphene-like two-dimensional materials," *Chemical Reviews* **113**, 3766–3798 (2013).
  - <sup>10</sup> Hua Zhang, "Ultrathin two-dimensional nanomaterials," *ACS Nano* **9**, 9451–9469 (2015).
  - <sup>11</sup> Alejandro Molina-Sánchez, Kerstin Hummer, and Ludger Wirtz, "Vibrational and optical properties of MoS<sub>2</sub>: From monolayer to bulk," *Surface Science Reports* **70**, 554 – 586 (2015).
  - <sup>12</sup> Fengcheng Wu, Fanyao Qu, and A. H. MacDonald, "Exciton band structure of monolayer MoS<sub>2</sub>," *Phys. Rev. B* **91**, 075310 (2015).
  - <sup>13</sup> Xi Ling, Han Wang, Shengxi Huang, Fengnian Xia, and Mildred S. Dresselhaus, "The renaissance of black phosphorus," *Proceedings of the National Academy of Sciences* **112**, 4523–4530 (2015).
  - <sup>14</sup> Alexandre Favron, Etienne Gaufrès, Frédéric Fossard, Anne-Laurence Phaneuf-L'Heureux, Nathalie YW Tang, Pierre L Lévesque, Annick Loiseau, Richard Leonelli, Sébastien Francoeur, and Richard Martel, "Photooxidation and quantum confinement effects in exfoliated black phosphorus," *Nature materials* **14**, 826–832 (2015).
  - <sup>15</sup> Fengnian Xia, Han Wang, Di Xiao, Madan Dubey, and Ashwin Ramasubramaniam, "Two-dimensional material nanophotonics," *Nature Photonics* **8**, 899–907 (2014), 1410.3882.
  - <sup>16</sup> G. Cassabois, P. Valvin, and B. Gil, "Hexagonal boron nitride is an indirect bandgap semiconductor," *Nature Photonics* **1**, 1–7 (2015), 1512.02962.
  - <sup>17</sup> P. Jaffrennou, J. Barjon, T. Schmid, L. Museur, A. Kanaev, J.-S. Lauret, C. Y. Zhi, C. Tang, Y. Bando, D. Golberg, B. Attal-Tretout, F. Ducastelle, and A. Loiseau, "Near-band-edge recombinations in multi-walled boron nitride nanotubes: Cathodoluminescence and photoluminescence spectroscopy measurements," *Phys. Rev. B* **77**, 235422 (2008).
  - <sup>18</sup> Romain Bourrellier, Michele Amato, Luiz Henrique Galvão Tizei, Christine Giorgetti, Alexandre Gloter, Malcolm I. Heggie, Katia March, Odile Stéphan, Lucia Reining, Mathieu Kociak, and Alberto Zobelli, "Nanometric Resolved Luminescence in h-BN Flakes: Excitons and Stacking Order," *ACS Photonics* **1**, 857–862 (2014).
  - <sup>19</sup> B. Arnaud, S. Lebègue, P. Rabiller, and M. Alouani, "Huge excitonic effects in layered hexagonal boron nitride," *Physical Review Letters* **96**, 026402 (2006).
  - <sup>20</sup> L. Wirtz, A. Marini, and A. Rubio, "Excitons in boron nitride nanotubes : dimensionality effects," *Physical Review Letters* **96**, 126104 (2006).
  - <sup>21</sup> Ludger Wirtz, Andrea Marini, Myrta Grüning, Claudio Attacalite, Georg Kresse, and Angel Rubio, "Comment on "Huge Excitonic Effects in Layered Hexagonal Boron Nitride"," *Phys. Rev. Lett.* **100**, 189701 (2008).

- <sup>22</sup> B. Arnaud, S. Lebègue, P. Rabiller, and M. Alouani, “Arnaud, Lebègue, Rabiller, and Alouani Reply;,” *Phys. Rev. Lett.* **100**, 189702 (2008).
- <sup>23</sup> Pierluigi Cudazzo, Lorenzo Sponza, Christine Giorgetti, Lucia Reining, Francesco Sottile, and Matteo Gatti, “Exciton band structure in two-dimensional materials,” *Phys. Rev. Lett.* **116**, 066803 (2016).
- <sup>24</sup> Thomas Galvani, Fulvio Paleari, Henrique P. C. Miranda, Alejandro Molina-Sánchez, Ludger Wirtz, Sylvain Latil, Hakim Amara, and François Ducastelle, “Excitons in boron nitride single layer,” *Phys. Rev. B* **94**, 125303 (2016).
- <sup>25</sup> R. F. Egerton, *Electron Energy-Loss Spectroscopy in the Electron Microscope 3rd Edition* (Springer US, 2011).
- <sup>26</sup> K. Sturm, “Dynamic structure factor: An introduction,” *Zeitschrift für Naturforschung A* **48**, 233–242 (1993).
- <sup>27</sup> S. Galambosi, L. Wirtz, J. A. Soininen, J. Serrano, A. Marini, K. Watanabe, T. Taniguchi, S. Huotari, A. Rubio, and K. Hämäläinen, “Anisotropic excitonic effects in the energy loss function of hexagonal boron nitride,” *Phys. Rev. B* **83**, 081413 (2011).
- <sup>28</sup> Giorgia Fugallo, Matteo Aramini, Jaakko Koskela, Kenji Watanabe, Takashi Taniguchi, Mikko Hakala, Simo Huotari, Matteo Gatti, and Francesco Sottile, “Exciton energy-momentum map of hexagonal boron nitride,” *Phys. Rev. B* **92**, 165122 (2015).
- <sup>29</sup> M. Haider, Stephan Uhlemann, Eugen Schwan, H. Rose, and Bernd Kabius, “Electron microscopy image enhanced,” *Nature* **392**, 768–769 (1998).
- <sup>30</sup> O.L. Krivanek, N. Dellby, and A.R. Lupini, “Towards sub-Å electron beams,” *Ultramicroscopy* **78**, 1–11 (1999).
- <sup>31</sup> M. Matijević, H. Stegmann, E. Essers, and G. Benner, “Recent Results of an in-column Energy Filter TEM with Monochromator,” *Microsc. Microanal.* **13(Suppl 2)**, 1160–1161 (2007).
- <sup>32</sup> D. A. Muller, L. Fitting Kourkoutis, M. Murfitt, J. H. Song, H. Y. Hwang, J. Silcox, N. Dellby, and O. L. Krivanek, “Atomic-scale chemical imaging of composition and bonding by aberration-corrected microscopy,” *Science* **319**, 1073–1076 (2008).
- <sup>33</sup> K. Suenaga and M. Koshino, “Atom-by-atom spectroscopy at graphene edge,” *Nature* **468**, 1088–1090 (2010).
- <sup>34</sup> C. Jeanguillaume and C. Colliex, “Spectrum-image: The next step in EELS digital acquisition and processing,” *Ultramicroscopy* **28**, 252–257 (1989).
- <sup>35</sup> L. Reimer, I. Fromm, and R. Rennekamp, “Operation modes of electron spectroscopic imaging and electron energy-loss spectroscopy in a transmission electron microscope,” *Ultramicroscopy* **24**, 339–354 (1988).
- <sup>36</sup> L. Reimer and R. Rennekamp, “Imaging and recording of multiple scattering effects by angular-resolved electron energy-loss spectroscopy,” *Ultramicroscopy* **28**, 258–265 (1989).
- <sup>37</sup> P. Wachsmuth, R. Hambach, M. K. Kinyanjui, M. Guzzo, G. Benner, and U. Kaiser, “High-energy collective electronic excitations in free-standing single-layer graphene,” *Phys. Rev. B* **88**, 075433 (2013).
- <sup>38</sup> T. Taniguchi and K. Watanabe, “Synthesis of high-purity boron nitride single crystals under high pressure by using Ba–BN solvent,” *Journal of Crystal Growth* **303**, 525–529 (2007).
- <sup>39</sup> R. D. Leapman, P. L. Fejes, and J. Silcox, “Orientation dependence of core edges from anisotropic materials determined by inelastic scattering of fast electrons,” *Phys. Rev. B* **28**, 2361–2373 (1983).
- <sup>40</sup> S. Saito, K. Higeta, and T. Ichinokawa, “Intensity analysis of boron and nitrogen k-edge spectra for hexagonal boron nitride by eels,” *Journal of Microscopy* **142**, 141–151 (1986).
- <sup>41</sup> N. Watanabe, H. Hayashi, Y. Udagawa, K. Takeshita, and H. Kawata, “Anisotropy of hexagonal boron nitride core absorption spectra by x-ray raman spectroscopy,” *Applied Physics Letters* **69**, 1370–1372 (1996).
- <sup>42</sup> R. Franke, S. Bender, J. Hormes, A.A. Pavlychev, and N.G. Fominych, “A quasi-atomic treatment of chemical and structural effects on k-shell excitations in hexagonal and cubic bn crystals,” *Chemical Physics* **216**, 243–257 (1997).
- <sup>43</sup> M. Jaouen, G. Hug, B. Ravel, A. L. Ankudinov, and J. J. Rehr, “Polarisation effects in hexagonal boron nitride near-edge structure: A real-space multiple scattering approach,” *EPL (Europhysics Letters)* **49**, 343 (2000).
- <sup>44</sup> R. Arenal, M. Kociak, and N. J. Zaluzec, “High-angular-resolution electron energy loss spectroscopy of hexagonal boron nitride,” *Applied Physics Letters* **90** (2007).
- <sup>45</sup> Yejun Feng, J. A. Soininen, A. L. Ankudinov, J. O. Cross, G. T. Seidler, A. T. Macrander, J. J. Rehr, and E. L. Shirley, “Exciton spectroscopy of hexagonal boron nitride using nonresonant x-ray raman scattering,” *Phys. Rev. B* **77**, 165202 (2008).
- <sup>46</sup> N. L. McDougall, R. J. Nicholls, and Partridge, “The near edge structure of hexagonal boron nitride,” *Microscopy and Microanalysis* **20**, 1053–1059 (2014).
- <sup>47</sup> Jian Wang, Zhiqiang Wang, Hyunjin Cho, Myung Jong Kim, T. K. Sham, and Xuhui Sun, “Layer speciation and electronic structure investigation of freestanding hexagonal boron nitride nanosheets,” *Nanoscale* **7**, 1718–1724 (2015).
- <sup>48</sup> G. Strinati, “Application of the green’s functions method to the study of the optical properties of semiconductors,” *La Rivista del Nuovo Cimento* (1978-1999) **11**, 1–86 (1988).
- <sup>49</sup> D Pacilé, M Papagno, T Skála, V Matolín, T Sainsbury, T Ikuno, D Okawa, A Zettl, and K C Prince, “Excitons at the b k edge of boron nitride nanotubes probed by x-ray absorption spectroscopy,” *Journal of Physics: Condensed Matter* **22**, 295301 (2010).
- <sup>50</sup> C. Tarrío and S. E. Schnatterly, “Interband transitions, plasmons, and dispersion in hexagonal boron nitride,” *Phys. Rev. B* **40**, 7852–7859 (1989).
- <sup>51</sup> P Moreau and MC Cheynet, “Improved comparison of low energy loss spectra with band structure calculations: the example of bn filaments,” *Ultramicroscopy* **94**, 293–303 (2003).
- <sup>52</sup> A.G. Marinopoulos, L. Wirtz, A. Marini, V. Olevano, A. Rubio, and L. Reining, “Optical absorption and electron energy loss spectra of carbon and boron nitride nanotubes: a first-principles approach,” *Applied Physics A* **78**, 1157–1167 (2004).
- <sup>53</sup> R J Nicholls, J M Perkins, V Nicolosi, D W McComb, P D Nellist, and J R Yates, “Low-loss eels of 2d boron nitride,” *Journal of Physics: Conference Series* **371**, 012060 (2012).
- <sup>54</sup> C. T. Pan, R. R. Nair, U. Bangert, Q. Ramasse, R. Jalil, R. Zan, C. R. Seabourne, and A. J. Scott, “Nanoscale electron diffraction and plasmon spectroscopy of single- and few-layer boron nitride,” *Phys. Rev. B* **85**, 045440 (2012).
- <sup>55</sup> Florence J. Nelson, Juan-Carlos Idrobo, John D. Fite, Zoran L. Mišković, Stephen J. Pennycook, Sokrates T. Pantelides, Ji Ung Lee, and Alain C. Diebold, “Electronic

- excitations in graphene in the 1–50 eV range: The  $\pi$  and  $\pi^*$  peaks are not plasmons,” *Nano Letters* **14**, 3827–3831 (2014).
- <sup>56</sup> Dino Novko, Vito Despoja, and Marijan Šunjić, “Changing character of electronic transitions in graphene: From single-particle excitations to plasmons,” *Phys. Rev. B* **91**, 195407 (2015).
- <sup>57</sup> S. C. Liou, C.-S. Shie, C. H. Chen, R. Breitwieser, W. W. Pai, G. Y. Guo, and M.-W. Chu, “ $\pi$ - plasmon dispersion in free-standing graphene by momentum-resolved electron energy-loss spectroscopy,” *Phys. Rev. B* **91**, 045418 (2015).
- <sup>58</sup> V U Nazarov, “Electronic excitations in quasi-2d crystals: what theoretical quantities are relevant to experiment?” *New Journal of Physics* **17**, 073018 (2015).
- <sup>59</sup> Giancarlo Cappellini, Guido Satta, Maurizia Palumbo, and Giovanni Onida, “Optical properties of bn in cubic and layered hexagonal phases,” *Phys. Rev. B* **64**, 035104 (2001).
- <sup>60</sup> G. Y. Guo and J. C. Lin, “Systematic *ab initio* study of the optical properties of bn nanotubes,” *Phys. Rev. B* **71**, 165402 (2005).
- <sup>61</sup> John P. Perdew, Kieron Burke, and Matthias Ernzerhof, “Generalized gradient approximation made simple,” *Phys. Rev. Lett.* **77**, 3865–3868 (1996).
- <sup>62</sup> J. J. Mortensen, L. B. Hansen, and K. W. Jacobsen, “Real-space grid implementation of the projector augmented wave method,” *Phys. Rev. B* **71**, 035109 (2005).
- <sup>63</sup> Hans-Christian Weissker, Jorge Serrano, Simo Huotari, Eleonora Luppi, Marco Cazzaniga, Fabien Bruneval, Francesco Sottile, Giulio Monaco, Valerio Olevano, and Lucia Reining, “Dynamic structure factor and dielectric function of silicon for finite momentum transfer: Inelastic x-ray scattering experiments and *ab initio* calculations,” *Phys. Rev. B* **81**, 085104 (2010).

**SUPPLEMENTARY MATERIAL OF : ANGULAR RESOLVED ELECTRON ENERGY LOSS SPECTROSCOPY IN HEXAGONAL BORON NITRIDE**

**A. HRTEM of FIB slabs**

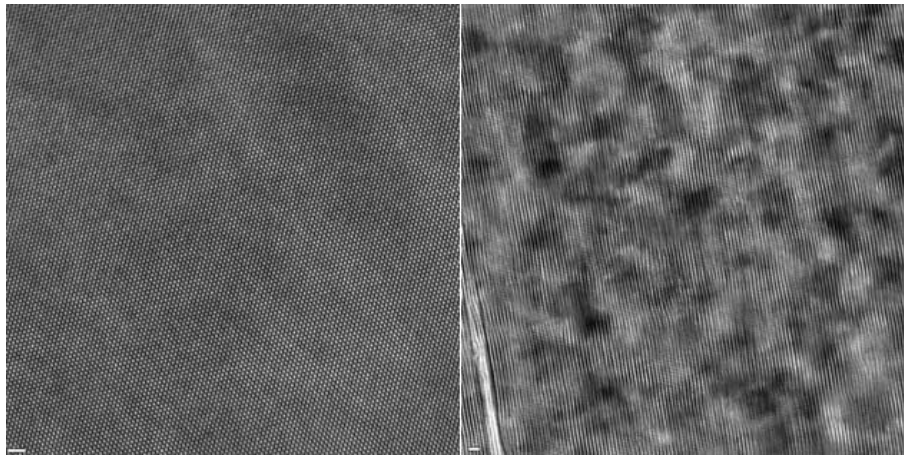


FIG. S1. High Resolution TEM image of samples prepared by FIB. Sample orientations correspond to (0001) zone axis (left) and (10 $\bar{1}$ 0) zone axis (right).

B.  $\omega - q$  map at the nitrogen  $K$  edge [0001] direction

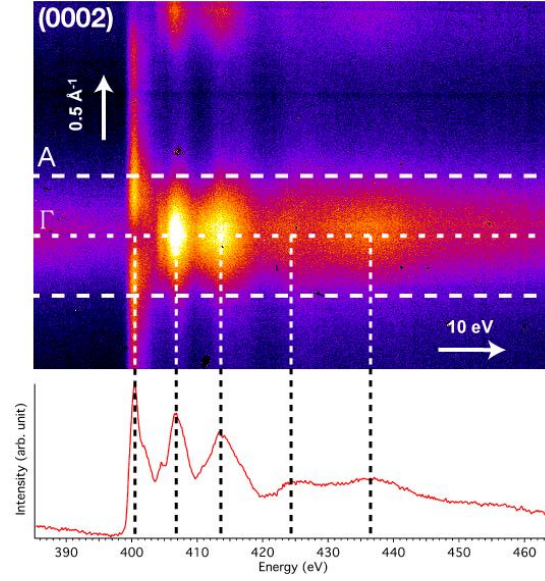


FIG. S2.  $\omega - q$  image recorded in the  $\Gamma A$  direction close to the nitrogen  $K$ -edge (400 eV). Dashed lines delimitate the Brillouin zone. Bottom : related EELS spectrum integrated over the whole Brillouin zone. The dotted line indicates the corresponding Brillouin zone section and significant edge structures.

### C. $\omega - q$ geometry versus crystal orientation

Loss spectra are very dependent on the orientation of the sample with respect to the electron beam. Details concerning the geometry used in the experiments are given here. As can be seen in Fig. S3, the zone axis is not

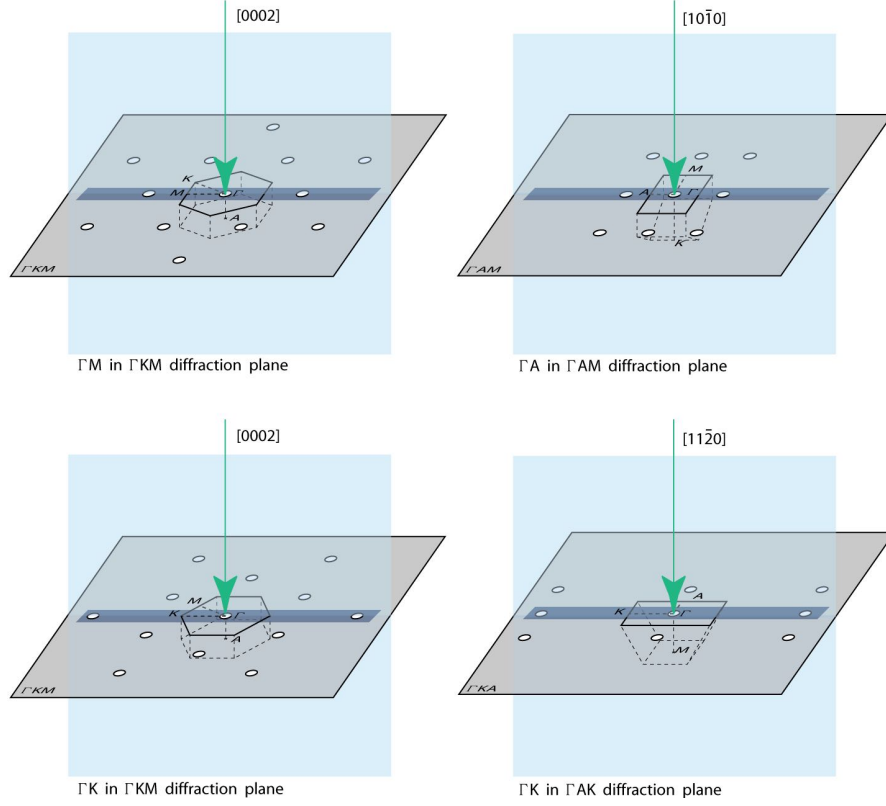


FIG. S3. Different instrumental geometries related to the crystal orientation (zone axis) and the direction of the slit at the entrance of the  $\Omega$  filter. The spectra in the  $\Gamma M$  and  $\Gamma K$  directions shown in the main text correspond to the  $[0002]$  zone axis (left). The spectrum in the  $\Gamma A$  direction corresponds to the  $[10\bar{1}0]$  axis.

sufficient to describe the geometry and one has also to precise the orientation of the slit used in  $\omega - q$  maps. The diffraction pattern of the sample as well as the Brillouin zone are shown in the Fig. S3. One can see that, depending on the geometry, it is possible to probe a direction with different components in and out of the diffraction plane. In the main text the spectra along  $\Gamma M$  and  $\Gamma K$  correspond to the  $[0002]$  zone axis (left). The spectrum along  $\Gamma A$  corresponds to the  $[10\bar{1}0]$  zone axis. Fig. S4 shows results obtained with geometries different from those in the main text. The results are identical for  $q \neq 0$  whereas there are differences in the  $q = 0$  spectrum because of the different components (*i.e.* Brillouin zone direction) mixed at  $q = 0$ .

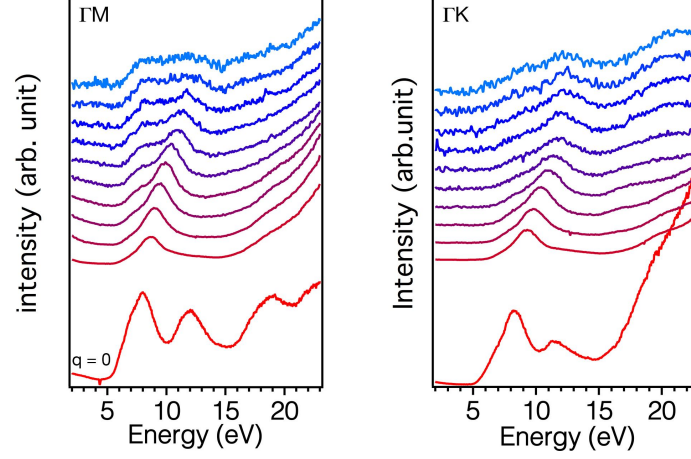


FIG. S4.  $\omega - q$  plot and EEL spectra multiplied by  $q^2$  (for  $q \neq 0$ ) along the  $\Gamma M$  and  $\Gamma K$  directions. Left : zone axis is  $[10\bar{1}0]$ , diffraction plane is  $(\Gamma MA)$ , slit is along  $[\Gamma M]$ . Right : zone axis is  $[11\bar{2}0]$ , diffraction plane is  $(\Gamma KA)$ , slit is along  $[\Gamma K]$ .

#### D. Benchmark EELS, NRIXS from Galambosi et al. and calculations from Fugallo et al.

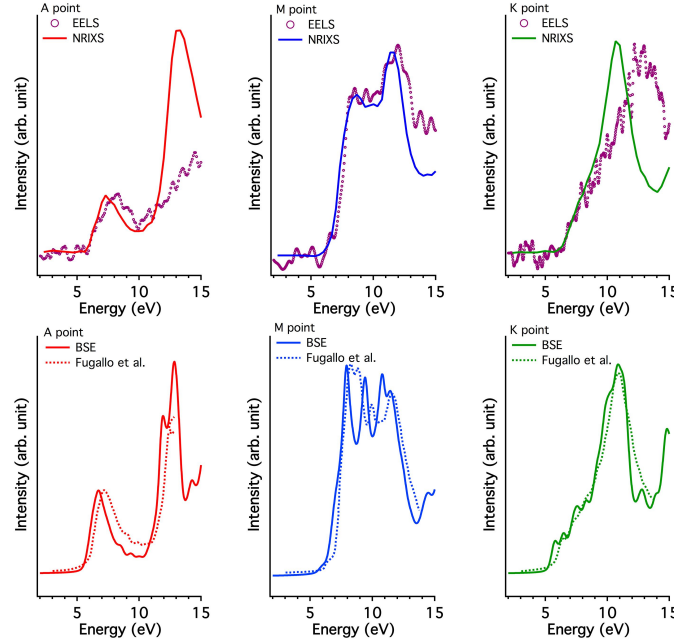


FIG. S5. Top: comparison between the present work (EELS) and NRIXS data extracted from Galambosi et al, Phys. Rev. B **83**, 081413 (2011) at A, M and K points in the Brillouin zone. Bottom: comparison between calculations performed in this work and those extracted from Fugallo et al, Phys. Rev. B **92**, 165122 (2015).

### E. Theoretical simulations and discussions

The dielectric matrix  $\epsilon_{GG'}(\mathbf{q}, \omega)$ , has been computed *ab-initio* in the random phase approximation (RPA) and by solving the Bethe-Salpeter equation (BSE). For the latter calculations, the quasiparticle corrections have been approximated by a scissor operator of 1.73 eV (value derived from the average GW correction of the HOMO-LUMO gap). More details on the computational parameters can be found on the main text.

In Fig. S6 we report the loss function extracted from  $\omega - \mathbf{q}$  maps along the high-symmetry lines  $\Gamma M$ ,  $\Gamma K$  and  $\Gamma A$  (dots) together with the dispersion of the RPA spectra along the same directions (solid lines). The agreement for in-plane components is very good in reproducing the main structures, not only at the zone borders but also all along the line. This observation provides an even stronger justification to the use of RPA in drawing the maps of Fig. 7 of the main text. On the other hand, we see that the same misalignment pointed for  $\mathbf{q} = A$  (see main text) is repeated all along the  $\Gamma A$  line, the offset being almost constant. Despite the wrong alignment, theory and experiment agree in predicting a basically dispersionless loss function for off-plane momentum transfer, a confirmation of the fact that plasmonic excitations are well confined on hBN planes.

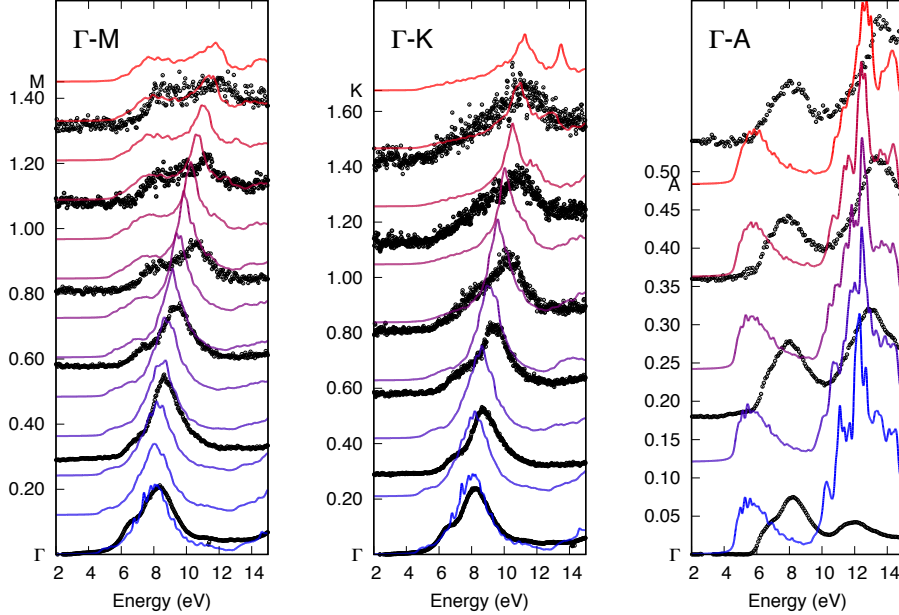


FIG. S6. RPA and experimental loss function (solid lines and bullets respectively) along high symmetry lines. On  $y$  axis units are  $\text{\AA}^{-1}$ .

To identify clearly the excitonic features from other effects, it is instructive to compare the BSE calculation to an independent-particle simulation stemming from the same band structure (we call it SO-RPA). To further reduce the source of discrepancies, we shall use the same  $q$ -point grid in both simulations. The resulting calculations are reported in Fig. S7, where solid lines have been computed on the same  $q$ -point grid, while the dashed red curves correspond to SO-RPA calculations on a denser  $q$ -point grid (respectively  $12 \times 12 \times 4(8)$   $k$ -points in the first case,  $24 \times 24 \times 8$  in the second).

In  $\mathbf{q} = A$  the main effect of the electron-hole interaction is a redshift of the spectral line of approximately 0.8 eV. This shift increases for higher energy, and approximately cancel the value of the scissor operator around 12 eV. Also for  $\mathbf{q} = K$  the excitonic effect is mainly a redshift of the structures, but the amount of the shift is approximately constant and similar to the scissor applied. Experimental spectra agree on the measure of a step-like onset. This feature is also predicted by BSE (arrow in Fig. S7), but it is absent in RPA calculations, which clearly indicates its excitonic nature. More peculiarities can be found in the spectrum at  $\mathbf{q} = M$ . Beside the usual in-plane shift already discussed, we observe here an important weight redistribution from high energy to low energy peaks. The letters in Fig. S7 help in tracing this redistribution. From the comparison between the two RPA calculations, we can state that the coarseness of the  $k$ -point used in the BSE calculation can lead to a slight overestimation of the spectral intensity, however this effect is globally negligible when main characteristics are of interest. The only severe exception are peaks  $D$  and  $F$  at  $\mathbf{q} = M$ , which result excessively enhanced when compared against the calculations by Fugallo.

We continue the analysis of the structures of the loss function by discussing the plasmonic nature of the peaks. Strictly speaking a plasmon resonance is found when  $\text{Re}[\epsilon(\omega)]$  vanishes. We can adopt though a less strict definition:

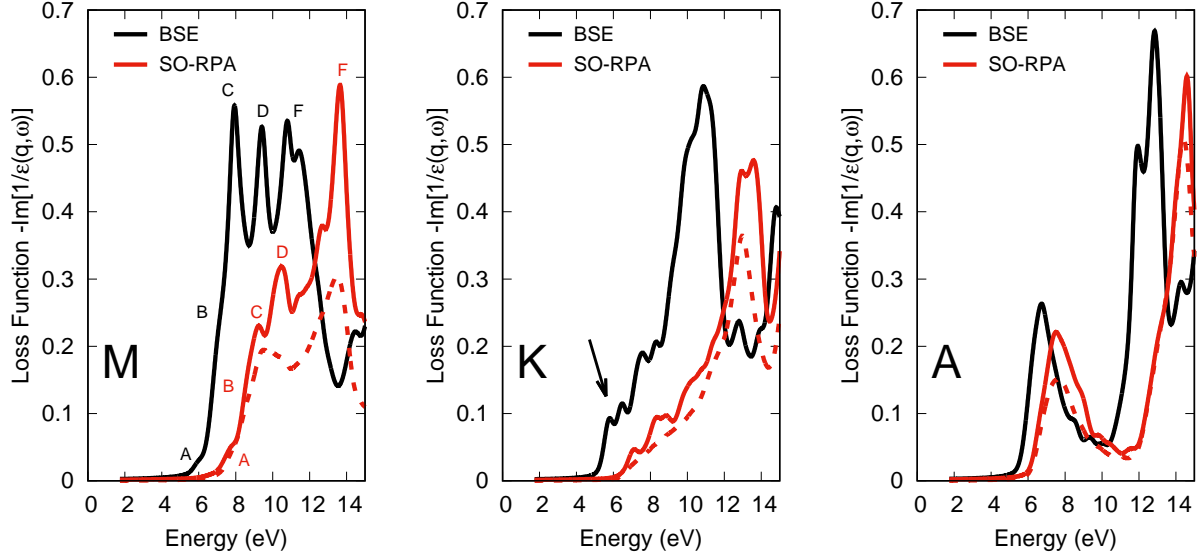


FIG. S7. Analysis of the excitonic structures at different momentum transfer.

When a peak of the loss function is due mainly to a reduction of  $\text{Re}[\epsilon(\omega)]$  (in absolute value), then the excitation has a predominant plasmonic character, when it is due to structures in  $\text{Im}[\epsilon(\omega)]$ , it has predominantly an inter-band transition character. In Fig. S8 we report the real and the imaginary parts of  $\epsilon$  in the upper panels and the loss function in the bottom panels for  $\mathbf{q} = M, K, A$ . From this analysis we can assert that the structures at 10 eV in  $K$ , the broad peak between 7 and 13 eV in  $M$  and at 12 eV in  $A$  have clearly a plasmonic nature, even though only the last one is a proper plasmon resonance. We would tend to associate a inter-band nature to the three peaks decorating the plasmon at  $M$ , and has a clear inter-band character the step-like onset at  $K$ . It is difficult instead to identify a predominant character in the structure at 7 eV at  $\mathbf{q} = A$ , that we would associate to some neutral excitation with mixed characteristics of a plasmonic and an inter-band excitation.

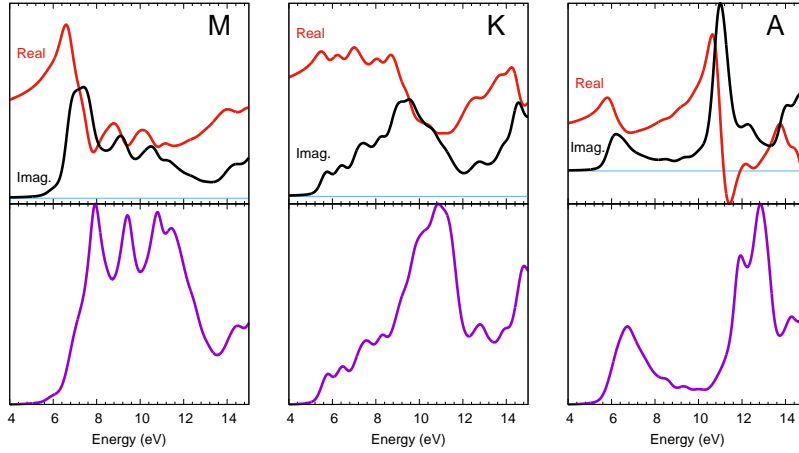


FIG. S8. Analysis of plasmonic excitations at different momentum transfer. Top: Real and imaginary part of the dielectric function  $\epsilon(\omega)$ . Bottom: Loss function equal to  $-\text{Im} \epsilon^{-1}(\omega)$ .

Finally we conclude the presentation of our theoretical results by reporting the BSE calculations at  $\mathbf{q} \approx 0$  for in-plane and out-of-plane components (Fig. S9).

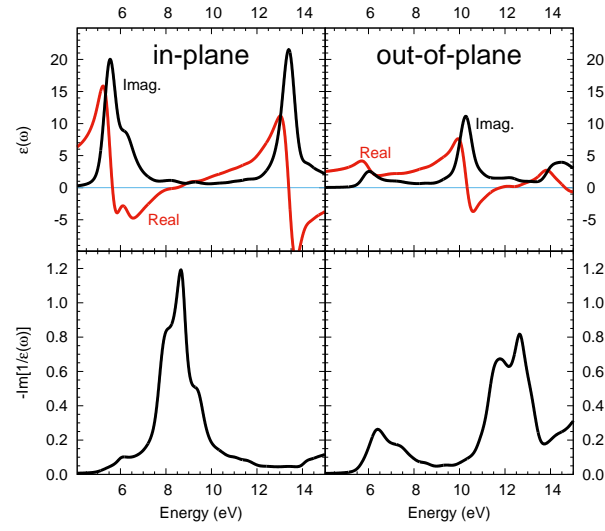


FIG. S9. Analysis of plasmonic excitations at  $\mathbf{q} \approx 0$ .